

Rapid Communication

Cite this article: Ibe CU, Langone A, Stuart FM, Brogi A, Caggianelli A, Liotta D, and Tursi F (2023) Rapid exhumation of young granites in an extensional domain: the example of the Giglio Island pluton (Tuscany). *Geological Magazine* **160**: 1241–1253. <https://doi.org/10.1017/S0016756823000420>

Received: 3 May 2023

Revised: 28 June 2023

Accepted: 30 June 2023








First published online: 3 August 2023

Keywords:

zircon U–Pb; apatite (U–Th)/He; magma emplacement; granite exhumation; Giglio Island

Corresponding author: Chinedu Uduma Ibe; Email: chinedu.ibe@uniba.it

Rapid exhumation of young granites in an extensional domain: the example of the Giglio Island pluton (Tuscany)

Chinedu Uduma Ibe¹ , Antonio Langone² , Finlay M. Stuart³ , Andrea Brogi^{1,4} , Alfredo Caggianelli¹ , Domenico Liotta^{1,4}  and Fabrizio Tursi⁵ 

¹Department of Earth and Geo-environmental Sciences, University of Bari Aldo Moro, Bari, Italy; ²Department of Earth and Environmental Sciences, University of Pavia, Pavia, Italy; ³Isotope Geosciences, Scottish Universities Environmental Research Centre, East Kilbride, UK; ⁴CNR-IGG, Institute of Geosciences and Earth Resources, Pisa, Italy and ⁵Department of Earth Sciences, University of Turin, Torino, Italy

Abstract

The presence of recently intruded granites at Earth's surface suggests that their exhumation may have occurred rapidly. The Neogene granites of the Tuscan Magmatic Province (Italy) were emplaced during a period of extensional tectonics and are ideal for determining and quantifying the exhumation process. The peraluminous monzogranite of Giglio Island in the northern Tyrrhenian Sea is characterized by the presence of roof pendants, xenoliths and mirolitic cavities. The petrologic study of metamorphic xenoliths and new zircon U–Pb ages show that the granite was emplaced at 6.4–10 km depth at 5.7 ± 0.4 Ma. Exhumation, constrained by apatite (U–Th)/He ages, was essentially complete in 0.9 Myr at a minimum rate of 6 mm/year. This requires rapid tectonic unroofing, isostatic rebound and thermal softening activity, weakening the upper crust and favouring exhumation at a previously undocumented rate.

1. Introduction

Granitic rocks that are now exposed at the surface, and emplaced in the upper crust during Neogene–Quaternary, bear witness to recent exhumation (e.g. Ito *et al.* 2013; Spencer *et al.* 2019; Spiess *et al.* 2021). Chronological constraints on cooling histories indicate that extremely high rates of tectonic exhumation are feasible, particularly during late orogenic extension (Zák *et al.* 2011; Hennig *et al.* 2017; Gardien *et al.* 2022), when crustal anatexis by decompression, detachment faults and thermo-rheological perturbation produced by the granitic intrusions are active (Daniel & Jolivet, 1995; Dallmeyer & Liotta, 1998; Acocella & Rossetti, 2002; Caggianelli *et al.* 2014; Jolivet *et al.* 2021). This widely accepted interplay has increased numerical modelling of exhumation using geochronological data (Dobson *et al.* 2010; Jiao *et al.* 2017), providing rates, from less than 1 mm/year (Lanari *et al.* 2023), up to 40 mm/year (Spencer *et al.* 2019). This wide spectrum of exhumation rates suggests the need to set up a robust and wide database of thermochronological data to better constrain the process. We contribute to this issue by providing data from the inner Northern Apennines (i.e. Northern Tyrrhenian Basin and Tuscany, Fig. 1), where post-extensional tectonics took place since early-middle Miocene (Carmignani *et al.* 1994; Carmignani *et al.* 1995; Carmignani *et al.* 2001; Brogi, 2005, 2008; Brogi & Liotta, 2008; Barchi, 2010), in association with coeval magmatism, referred to as the Tuscan Magmatic Province (TMP) (Serri *et al.* 1993; Poli *et al.* 2002).

The TMP includes Neogene felsic plutons (Fig. 1) that were mostly emplaced at less than 8 km depth (e.g. Innocenti *et al.* 1992, 2005; Brogi *et al.* 2021; Di Vincenzo *et al.* 2022). Several plutons are exposed while others have been encountered at a depth of 3–4 km during drilling works for geothermal and mining exploitations (e.g. Ricceri & Stea, 1992; Gianelli & Laurenzi, 2001), as in the case of the Larderello area (e.g. Dini *et al.* 2005; Gola *et al.* 2017; Romagnoli *et al.* 2010; Rochira *et al.* 2018, Montanari *et al.* 2023). Therefore, the northern Tyrrhenian Sea and southern Tuscany represent ideal crustal sectors for studying and quantifying the exhumation processes that led to the exposure of the Neogene felsic plutons (Fig. 1a). In this paper, we integrate petrological, geochronological and thermochronological analyses of the granite exposed in the Giglio Island, with the aim of constraining the exhumation history of the pluton in the framework of the extensional tectonics that formed the Northern Tyrrhenian basin (Fig. 1b). We hope the results of this research will arouse interest in the study of the processes that take place on the roof of granites and determine localized rapid exhumation.

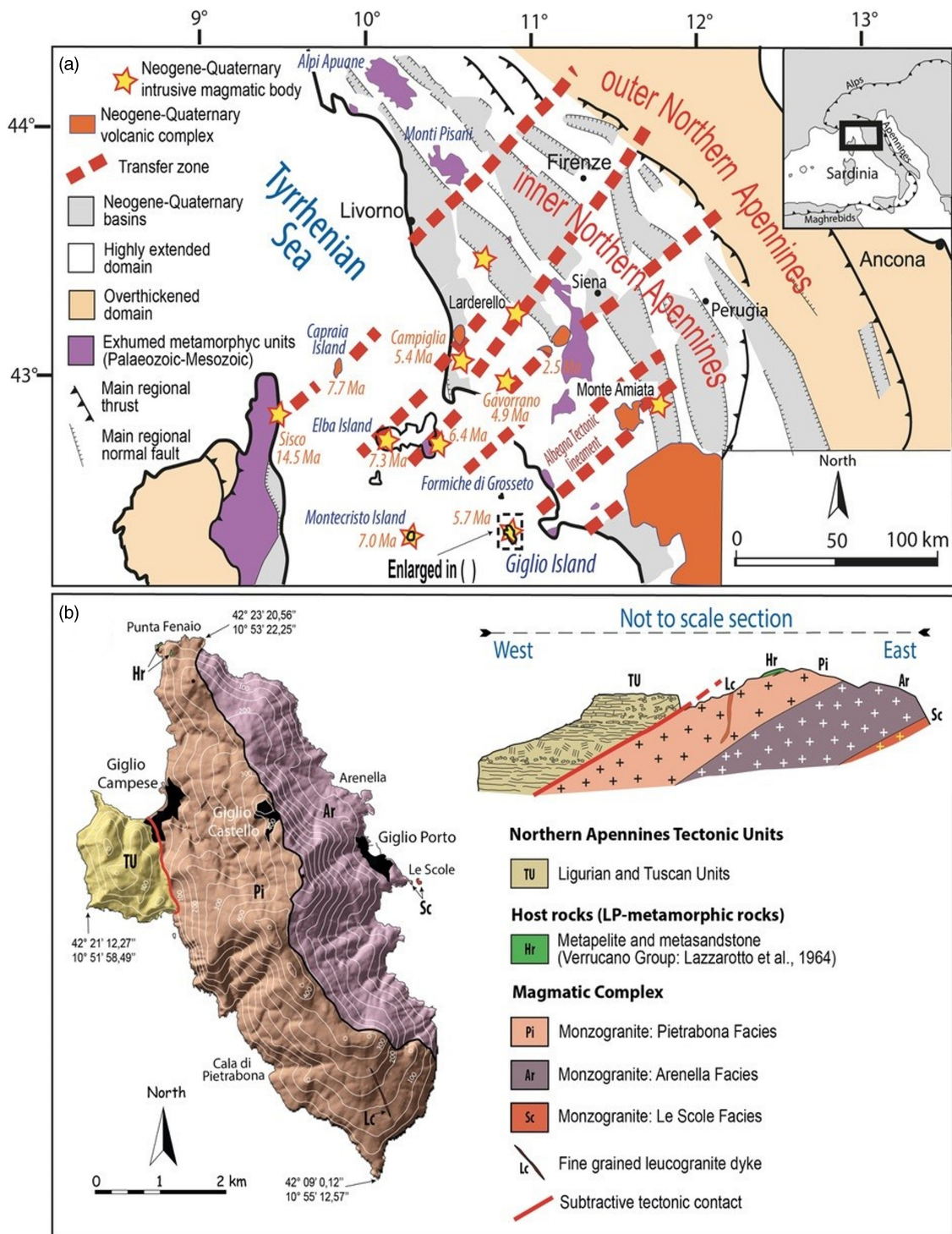


Figure 1. (a) Simplified geological map of the Northern Apennines and Northern Tyrrhenian Sea. The main Pliocene–Quaternary basins, transfer zones (See Brogi *et al.* 2021), Neogene–Quaternary volcanic complexes and main intrusive magmatic bodies and metamorphic units are shown. The ages of the main granites of Campiglia ($^{40}\text{Ar}/^{39}\text{Ar}$; Di Vincenzo *et al.* 2022), Porto Azzurro in eastern Elba (zircon U–Pb; Spiess *et al.* 2021), Monte Capanne in western Elba (zircon U–Pb; Barboni *et al.* 2015), Gavorrano (biotite K–Ar; Ferrara & Tonarini, 1985), Montecristo (biotite K–Ar; Borsi *et al.*, 1967) and Capraia (biotite K–Ar; Aldighieri *et al.* 1998) are shown. (b) Geological sketch map of the Giglio Island (modified after Westerman *et al.* 1993). The facies of the monzogranite, as well as the units affected by high-pressure metamorphism, are shown. The cross-section shows the geometrical relations between the facies of the monzogranite.

2. Geological setting

Giglio Island (c. 21 km²) sits on the NNW trending Giglio–Formiche di Grosseto Ridge (Fig. 1a). It developed during Neogene extensional tectonic activity that was a consequence of post-collisional evolution

of the Northern Apennines (Bartole, 1995). The island is largely formed of peraluminous granite (Westerman *et al.* 1993), exposed in a roughly elliptical shape having a long axis of c. 9 km. The remaining part, the Franco promontory, is comprised of piled

tectonic units of the Northern Apennines belt (Lazzarotto *et al.* 1964) that were affected by high-pressure metamorphism (Capponi *et al.* 1997; Rossetti *et al.* 1999; Giuntoli & Viola, 2022). The Giglio pluton is a monzogranite (Westerman *et al.* 1993) composed of two main facies: a) the Arenella facies, a massive, K-feldspar megacryst-bearing granite that is exposed in the eastern part of the island and b) the Pietrabona facies, a foliated granite with a higher colour index that crops out mainly in the western part of the island and is juxtaposed with the metamorphic units by a tectonic contact that is interpreted as a dipping to the West normal fault (Lazzarotto *et al.* 1964; Rossetti *et al.* 1999). A smaller, more differentiated mass (Le Scole granite facies) intruded the main plutonic body and is characterized by an even stronger peraluminosity. It crops out near the East coast of the island, and at Le Scole islets, about 1 km to the southeast of Giglio Porto. Magmatic and metamorphic xenoliths (Barrese *et al.* 1987) are scattered throughout the granite, while small outcrops of the wall rock, affected by contact metamorphism, are exposed in the north of the island (Fig. 1b).

Eight samples from the main granite body, the minor Le Scole intrusion, a felsic dyke and a magmatic xenolith were dated by Rb–Sr biotite–whole-rock method by Westerman *et al.* (1993). They provided Rb–Sr whole rock–biotite cooling ages ranging from 4.88 ± 0.07 to 5.07 ± 0.08 Ma, not significantly different from previous K–Ar and Rb–Sr ages (5.1 ± 0.15 Ma; Ferrara & Tonarini, 1985). Westerman *et al.* (1993) reported Sr and Nd isotopic data that indicate the hybrid nature of the magma, generated by interaction of a crustal anatexis component and a subcrustal basic magma. On the basis of the normative composition of the monzogranite, plotted in the ternary Qtz–Ab–Or diagram for minimum melt composition in water-saturated conditions, they estimated crystallization pressure of the magma of c. 400 MPa, considerably higher than that estimated for the emplacement of other granites of the TMP (Monte Capanne and Porto Azzurro from Elba Island, Campiglia and Gavorrano localities; cfr. Musumeci & Vaselli, 2012; Caggianelli *et al.* 2018; Brogi *et al.* 2021; Di Vincenzo *et al.* 2022).

The geodynamic setting, which assisted the emplacement of the Giglio monzogranite, is characterized by a severe crustal stretching and lithospheric thinning (Carmignani *et al.* 1994; Di Stefano *et al.* 2011; Moeller *et al.* 2013), accompanied by top-to-the East extensional detachments and normal faults since early Miocene (Keller & Piali, 1990; Bartole, 1995; Carmignani *et al.* 1995; Jolivet *et al.* 1998; Rossetti *et al.* 1999; Jolivet *et al.* 2021). The final uplift and unroofing of the pluton took place during late Pliocene–early Pleistocene (Rossetti *et al.* 1999). The abundance of metamorphic xenoliths and xenocrysts and the presence of roof pendants in granite suggest that it was emplaced at less than 400 MPa (Clarke, 1992; Philpotts & Ague, 2022). Thus, there is uncertainty in the level of granite emplacement, and, in addition, there is no knowledge of the exhumation history. Consequently, to quantify the process that exposed the Giglio granite, we have estimated its emplacement level, by analysing metamorphic xenoliths, xenocrysts and wall rocks of the pluton, and obtained U–Pb and (U–Th)/He dates from the granite. These data have allowed us to trace the history from emplacement to exhumation of the pluton, in the regional tectonic framework of the inner Northern Apennines.

3. Analytical procedure

Preliminary observation of thin sections under the microscope was followed by BSE and EDS imaging performed at the Dipartimento di Scienze della Terra e Geambientali of the University of Bari.

Mineral compositions (Table S1) were obtained with energy dispersion systems (EDS) with X-Max Silicon drift detector from Oxford instruments coupled with a Zeiss EVO 50 XVP SEM. The operating conditions include 1 nA probe current, 100 s counting time, 8.5 mm working distance and 15 kV accelerating potential.

Zircon U–Pb ages were determined by LA-ICP-MS at CNR-IGG-UOS of Pavia, Italy. Zircons were separated by conventional methods (crushing, heavy liquids and handpicking) from one sample (GIG11). Prior to age determination, the internal structure of the zircon grains was investigated with backscattered electron (BSE) and cathodoluminescence (CL) images using a Philips XL30 electron microscope equipped with a Centaurus CL detector. Images were obtained using 15 kV acceleration and a working distance of 26 mm. Age determinations were made using a 193 nm ArF excimer laser microprobe (GeoLas200QMicrolas) coupled to a Triple Quadrupole (Agilent 8900). Analyses were carried out in single spot mode and with a spot size fixed at 25 μm . The laser was operated with a frequency of 5 Hz and with a fluence of 8 J/cm². Sixty seconds of background signal and at least 30 s of ablation signal were acquired. The signals of ²⁰²Hg, ²⁰⁴(PbHg), ²⁰⁶Pb, ²⁰⁷Pb, ²⁰⁸Pb, ²³²Th and ²³⁸U were acquired. ²³⁵U is calculated from ²³⁸U based on the mean ratio ²³⁸U/²³⁵U of 137.818 (Hiess *et al.* 2012). Masses 202 and 204 were measured to monitor the presence of common Pb. Mass bias and laser-induced fractionation were corrected by analysis of the GJ-1 zircon standard (608.56 ± 0.4 Ma; Jackson *et al.* 2004). The Plešovice zircon (Sláma *et al.* 2008) was analysed together with unknowns for quality control. Data were reduced using the GLITTER software package (Van Acherbergh *et al.* 2001). Time-resolved signals were carefully inspected to detect perturbation of the signal related to inclusions, cracks or mixed-age domains. Within the same analytical run, the error associated with the reproducibility of the external standards was propagated to each analysis of sample (see Horstwood *et al.* 2003), and after this procedure, each age determination was retained as accurate within the quoted error. Ages were calculated using the function in the software package Isoplot/Ex 3.00 (Ludwig, 2003). The discordance has been calculated as $\{[1 - ({}^{206}\text{Pb}/{}^{238}\text{U} \text{ age})/{}^{207}\text{Pb}/{}^{235}\text{U} \text{ age}]\} \times 100$. Analytical errors are reported as 2 σ . The IsoplotR software (Vermeesch, 2018) was used to draw diagrams of age data and to calculate the weighted average age. The 2 σ error of the weighted average age has been calculated as the statistical average of the 2 σ analytical error. U–Pb isotope data and calculated ages are reported in the data repository (Table 1).

The (U–Th)/He dating of apatite was carried out at the Scottish Universities Environmental Research Centre (SUERC), United Kingdom. The analytical protocol follows Foeken *et al.* (2006). Apatite crystals free from inclusions and cracks were selected using a high magnification (up to 500 \times) binocular polarising microscope. The grains with inclusions were easy to observe when the mineral is oriented in an extinction position. Zircon and monazite inclusions are typically very small and were located close to a few of the apatite crystal faces. All selected apatite grains were ≥ 80 μm radius with one or two terminations and a good crystal morphology. Two crystals with consistent diameter (to ensure equal diffusion and ejection characteristics) were put in a single Pt packet and crimped shut to prevent loss of crystals during heating. The Pt-foil packets were loaded directly into the sample planchet and mounted in the laser pan. Samples were heated for 120 seconds at approximately 600 $^{\circ}\text{C}$ using a 5.8 W beam on a 500 μm circle spot size delivered by a fibre diode laser. This procedure is enough to degas the crystals without volatilizing the U and Th. Evolved gases were purified using two liquid N₂-cooled traps and ⁴He amount

Table 1. LA-ICP-MS isotopic data of zircon from Giglio granite

Identifier	Zrc#	Spot	Zoning	Data for Wetherill plot ³							Ages ³						
				²⁰⁷ Pb/ ²⁰⁶ Pb	1 σ %	²⁰⁷ Pb/ ²³⁵ U	1 σ %	²⁰⁶ Pb/ ²³⁸ U	1 σ %	Rho	²⁰⁷ Pb/ ²⁰⁶ Pb	1 σ abs	²⁰⁷ Pb/ ²³⁵ U	1 σ abs	²⁰⁶ Pb/ ²³⁸ U	1 σ abs	% U-Pb disc ^d
006SMPL	Zrc1	rim	Homogenous	0.06	0.01	0.01	0.00	0.00	0.00	0.0	666	74	7	1	5.2	0.2	25.1*
007SMPL	Zrc2	rim	Homogenous	0.05	0.01	0.01	0.00	0.00	0.00	0.0	104	16	6	1	5.8	0.3	4.0
008SMPL	Zrc3	rim	Oscillatory	0.05	0.01	0.01	0.00	0.00	0.00	0.1	182	20	6	1	5.7	0.2	6.8
013SMPL	Zrc8	rim	Homogenous	0.05	0.00	0.01	0.00	0.00	0.00	0.0	208	20	6	1	5.6	0.1	7.7
014SMPL	Zrc9	rim	Homogenous	0.05	0.00	0.01	0.00	0.00	0.00	0.0	165	14	6	0	5.4	0.1	6.9*
015SMPL	Zrc10	rim	Oscillatory	0.05	0.01	0.01	0.00	0.00	0.00	0.0	81	13	6	1	5.5	0.3	2.8
016SMPL	Zrc11	rim	Oscillatory	0.05	0.01	0.01	0.00	0.00	0.00	0.0	19	2	6	1	5.5	0.2	0.9
018SMPL	Zrc14	core	Homogenous	0.06	0.00	0.01	0.00	0.00	0.00	0.0	414	37	7	1	5.5	0.1	15.8
020SMPL	Zrc15	rim	Oscillatory	0.08	0.01	0.01	0.00	0.00	0.00	0.0	1184	193	10	2	6.0	0.3	41.6*
021SMPL	Zrc16	rim	Homogenous	0.05	0.00	0.01	0.00	0.00	0.00	0.0	362	33	7	1	5.8	0.1	14.0
027SMPL	Zrc17	rim	Oscillatory	0.05	0.01	0.01	0.00	0.00	0.00	0.0	249	33	7	1	5.9	0.2	10.0
028SMPL	Zrc19	rim	Oscillatory	0.05	0.00	0.01	0.00	0.00	0.00	0.1	69	3	6	0	5.6	0.1	3.0
029SMPL	Zrc20	rim	Oscillatory	0.05	0.00	0.01	0.00	0.00	0.00	0.0	102	9	6	0	5.6	0.1	4.2
030SMPL	Zrc21	rim	Homogenous	0.05	0.01	0.01	0.00	0.00	0.00	0.0	322	58	7	1	5.7	0.3	12.3
031SMPL	Zrc22	rim	Oscillatory	0.08	0.02	0.01	0.00	0.00	0.00	0.0	1266	274	9	2	5.0	0.3	44.4*
032SMPL	Zrc23	rim	Oscillatory	0.05	0.00	0.01	0.00	0.00	0.00	0.0	83	5	6	0	5.9	0.1	3.5
034SMPL	Zrc25	rim	Oscillatory	0.05	0.00	0.01	0.00	0.00	0.00	0.0	107	10	6	1	5.6	0.1	3.9
035SMPL	Zrc27	rim	Oscillatory	0.05	0.00	0.01	0.00	0.00	0.00	0.1	34	2	6	0	5.9	0.1	1.3
036SMPL	Zrc28A	rim	Oscillatory	0.05	0.00	0.01	0.00	0.00	0.00	0.1	85	6	6	0	5.6	0.1	3.2
037SMPL	Zrc28B	rim	Homogenous	0.05	0.01	0.01	0.00	0.00	0.00	0.0	230	26	6	1	5.8	0.2	9.2
038SMPL	Zrc29	rim	Homogenous	0.06	0.01	0.01	0.00	0.00	0.00	0.0	439	41	7	1	6.0	0.2	16.6*
039SMPL	Zrc30	rim	Oscillatory	0.06	0.01	0.01	0.00	0.00	0.00	0.0	503	81	7	1	5.8	0.3	19.7
041SMPL	Zrc32	rim	Homogenous	0.05	0.00	0.01	0.00	0.00	0.00	0.1	200	14	6	0	5.5	0.1	7.7
042SMPL	Zrc33	rim	Oscillatory	0.05	0.01	0.01	0.00	0.00	0.00	0.0	192	27	7	1	6.1	0.2	7.4
048SMPL	Zrc34	rim	Oscillatory	0.06	0.01	0.01	0.00	0.00	0.00	0.0	444	87	8	1	6.3	0.3	17.1*
050SMPL	Zrc36	rim	Oscillatory	0.06	0.00	0.01	0.00	0.00	0.00	0.0	657	51	7	1	5.2	0.1	25.2*
051SMPL	Zrc37	core	Homogenous	0.05	0.00	0.13	0.01	0.02	0.00	0.1	228	16	128	8	123	3	4.1*
052SMPL	Zrc37	rim	Homogenous	0.05	0.00	0.20	0.01	0.03	0.00	0.1	280	16	188	10	181	4	3.8*
053SMPL	Zrc38	rim	Oscillatory	0.05	0.00	0.01	0.00	0.00	0.00	0.0	352	29	6	1	5.5	0.1	13.5
054SMPL	Zrc40	rim	Oscillatory	0.05	0.00	0.01	0.00	0.00	0.00	0.0	8	1	6	0	5.7	0.1	-0.5

(Continued)

Table 1. (Continued)

055SMPL	Zrc41	rim	Oscillatory	0.05	0.00	0.01	0.00	0.00	0.00	0.0	145	14	6	1	5.6	0.1	6.1
057SMPL	Zrc43	rim	Oscillatory	0.05	0.01	0.01	0.00	0.00	0.00	0.0	36	5	6	1	5.8	0.2	1.4
058SMPL	Zrc45	rim	Oscillatory	0.06	0.01	0.01	0.00	0.00	0.00	0.0	634	96	8	1	5.9	0.3	24.2
059SMPL	Zrc46	rim	Oscillatory	0.05	0.01	0.01	0.00	0.00	0.00	0.0	218	29	6	1	5.6	0.2	8.5
061SMPL	Zrc48	rim	Oscillatory	0.05	0.00	0.01	0.00	0.00	0.00	0.1	252	18	6	0	5.7	0.1	9.8
062SMPL	Zrc50	rim	Oscillatory	0.05	0.01	0.01	0.00	0.00	0.00	0.0	137	17	6	1	5.7	0.2	5.4

*=not considered for the weighted average age calculation.

was determined using a Hidden HAL3F quadrupole mass spectrometer. Blank He amounts were determined by heating empty Pt-foil packets before each sample. All sample packets were re-heated to ensure that all ^4He was extracted in the heat step. After the ^4He analysis, the aliquots were retrieved from the pan. All samples were then spiked with approximately 0.05 g ^{230}Th and 0.02 g ^{235}U , and the volume was made up to 4 ml with 5% ultra-pure HNO_3 . The solutions were then equilibrated for 24 hours on a hot plate at 80 °C before being transferred into a vial for U and Th measurement. U and Th analysis were carried out on a VG Plasma Quad PQ2 + ICP-MS. Fractionation was monitored using the U500 standard with a certified value of $^{235}\text{U}/^{238}\text{U} = 0.9997$. A 5% HNO_3 wash-out solution was used to purge the ICP-MS between sample solution analyses. Total amounts of U and Th were determined following the formula of Evans *et al.* (2005), and final AHe ages were calculated using the noniterative formula of Meesters and Dunai (2005). Five aliquots of Durango apatite were analysed in each pan as an internal procedural standard. The average AHe age of these Durango apatite fragments (31.9 ± 2.3 Ma) is consistent and comparable to published age (31.0 ± 1.0 Ma; Boyce & Hodges, 2005; McDowell *et al.* 2005).

4. Emplacement depth

The wall rocks of the Giglio granite crop out in a limited area along the northern coast close to the lighthouse of Punta Fenaio (Fig. 1b). In addition, Westerman *et al.* (1993) reported the presence of rocks affected by contact metamorphism that they interpreted as roof pendants within the granite. The wall rocks consist of dark foliated metamorphic rocks derived from the Triassic pelitic and quartzitic sandstone of the Tuscan Domain (i.e. Verrucano Group, Lazzarotto *et al.* 1964). These metamorphic rocks are characterized by andalusite with quartz, K-feldspar, plagioclase, tourmaline, graphite, Fe-oxides and low content of micas \pm cordierite. Andalusite is mostly prismatic chiastolite that may reach a centimetre in length. Zones affected by advanced pinitization reflect the former presence of cordierite. These rocks can be classified as andalusite-tourmaline paragneiss and are not suitable for constraining the pressure range at the time of granite emplacement.

The granite of Giglio Island contains many xenoliths and xenocrysts mostly derived from the disaggregation of wall and roof rocks affected by contact metamorphism. This is particularly the case of the Arenella granite facies that contains isolated crystals of cordierite and miarolitic cavities with walls covered by quartz and tourmaline. The xenoliths are typically a few centimetres in size. They are characterized by the presence of andalusite and/or sillimanite, biotite, spinel, ilmenite, plagioclase, K-feldspar and cordierite. Ovoidal cordierite poikiloblasts with inclusions of biotite, green-brown spinel, fibrolite sheafs, ilmenite and minor blueish corundum (Fig. 2a). These characteristics are compatible with a metamorphic restitic or a magmatic peritectic genesis of cordierite (see Clarke, 1995). On the other hand, the presence of coarse-grained andalusite in wall rocks and roof pendants indicates that the andalusite-bearing xenoliths and xenocrysts are products of disaggregation of the wall rocks affected by contact metamorphism (Barrese *et al.* 1987). One andalusite-bearing xenolith is migmatitic and has thin melanocratic layers alternated with leucocratic feldspar-rich layers (Fig. 2b) (Pattison & Harte, 1988). The melanocratic layers are largely composed of biotite and elongated spinel-bearing mineral aggregates that in some cases show the presence of colourless or pinkish andalusite in the core (Fig. 2b). Corundum and zoned tourmaline surrounded by a feldspar shell are also present. Biotite is frequently embayed and is strongly pleochroic (Fig. 2c) up to saturated red-brown tones corresponding to elevated Ti content ($X_{\text{Ti}} = 0.53$, Table S1). The most remarkable feature is represented by the elongated mineral aggregates with a contour showing evidence of resorption. They host weakly pleochroic low-Ti biotite ($X_{\text{Ti}} = 0.01$). In some cases, hercynitic spinel grains ($X_{\text{Hc}} = 0.82$) host inclusions of corundum (Fig. 2b). The mineral aggregates are surrounded by plagioclase ($X_{\text{An}} = 0.38$), which in turn is surrounded by cloudy K-feldspar grains. The overall microstructural features indicate that biotite and andalusite were involved as reactants in partial melting.

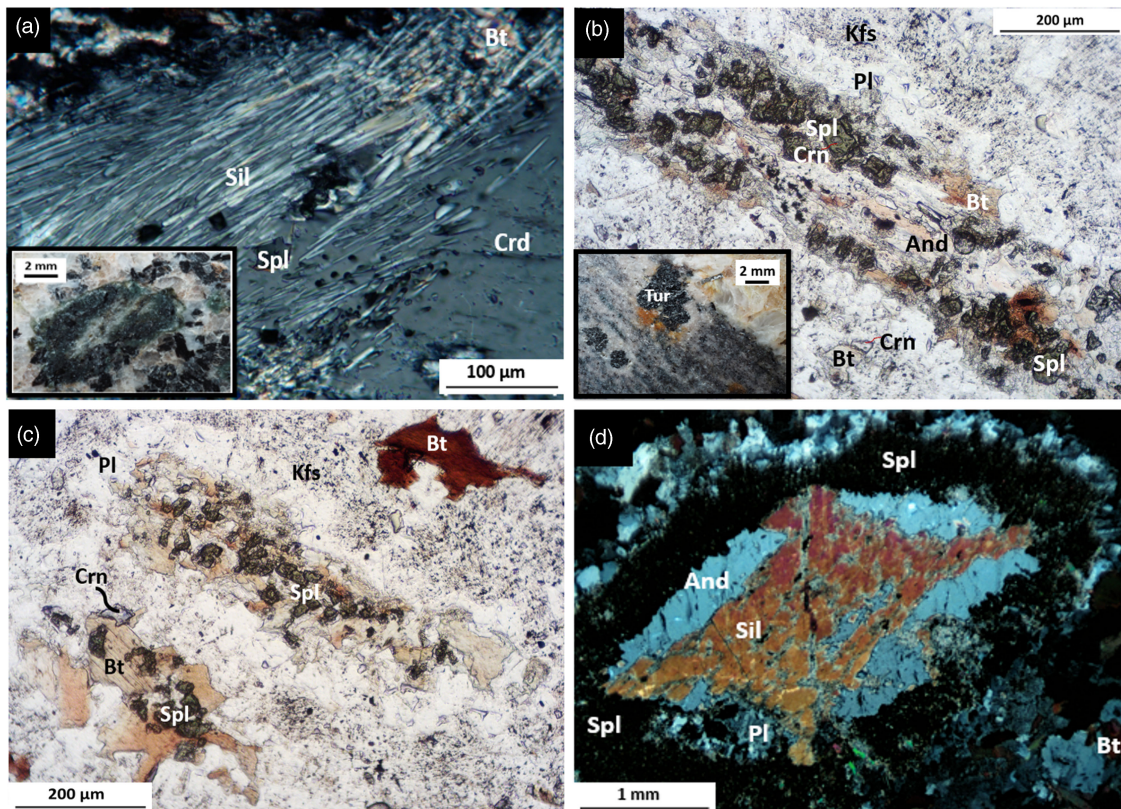
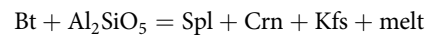


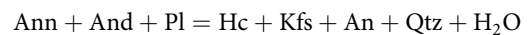
Figure 2. Micrographs of xenoliths and a xenocryst from the Giglio Island granite. Mineral abbreviations after Kretz (1983). (a) Thin section micrograph of xenolith showing poikiloblastic cordierite hosting fibrolite sheafs (Sil) and biotite, spinel + ilmenite and corundum (crossed polarized light). The inset shows the ovoid shape of the xenolith. (b) Thin section micrograph of andalusite-bearing xenolith showing an elongated mineral aggregate made up of spinel, biotite, corundum and, in the core, pinkish andalusite (plane-polarized light). It is surrounded by plagioclase and K-feldspar. The inset shows the laminated structure of the xenolith marked by thin melanocratic levels alternated with leucocratic feldspars-rich levels. The presence of tourmaline with embayed margins can be also observed. (c) Thin section micrograph of spinel – biotite – rich mineral aggregates and an isolated biotite with evident embayed margins (plane-polarized light). Biotite in the aggregate shows pale pleochroism in comparison to the isolated embayed crystal, reflecting the contrast in the Ti content, higher in the latter. The elongated mineral aggregate in the centre of the image is surrounded by plagioclase and turbid K-feldspar. (d) Thin section micrograph of an andalusite xenocryst in basal section affected by partial replacement with sillimanite mostly along the chiasmatic cross (cross-polarized light). The xenocryst is armoured by spinel-rich corona with plagioclase, minor biotite and corundum.

Evidence of partial melting was also observed in columnar xenocrysts of andalusite up to 2.5 cm in length. They are characterized by partial sillimanite replacement (see also Cesare *et al.* 2002) that, in basal section, occurred preferentially along the chiasmatic cross (Fig. 2d). They are armoured by a spinel-rich ($X_{Hc} = 0.81$) corona with plagioclase ($X_{An} = 0.36$), minor biotite and corundum. Locally, a spinel-plagioclase symplectite is observed. Outside the spinel-rich armour, plagioclase, cordierite and then K-feldspar occur. These microstructures have been found in wall rocks close to the contact with the magma (e.g. Johnson *et al.* 2004; Droop & Moazzen, 2007; Saki, 2010). Hence, the andalusite-bearing xenoliths and xenocrysts of the Giglio granite, after disaggregation from wall and roof rocks, underwent partial melting upon incorporation into the magma (Barrese *et al.* 1987). Thus, they are useful for our purpose of defining the level of emplacement of the Giglio Island granite.

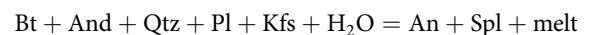
Several partial melting reactions in the K_2O -FeO-MgO- Al_2O_3 - SiO_2 - H_2O (KFMASH) system relevant for quartz-absent assemblages have been reported for the wall rocks and xenoliths of an igneous complex (see Pattison & Harte, 1988). Among these, a biotite $\pm Al_2SiO_5$ consuming reaction, compatible with our observations, is:



Since plagioclase is involved, we consider equilibria in systems including Na_2O and CaO as additional components. Thus, the first hercynite-forming reaction, R1, into NCKFASH system (Fig. 3), is:



At higher temperature, for SiO_2 -saturated compositions in the NCKFMASH system, the wet solidus reaction curve, R2, is encountered:



Reaction R2 degenerates in the NCKFASH system (Fig. 3) at high-P, in the sillimanite stability field, with the degenerate point representing the maximum-P for the entrapment of the xenolith. The position of the wet solidus is sensitive to the presence of boron in the fluid phase (e.g. Pichavant, 1981). Embayed margins of tourmaline imply that it has been consumed with the consequent release of boron. The effect on the solidus is shown in Fig. 3 (modified from Fig. 1 in Spicer *et al.* 2004).

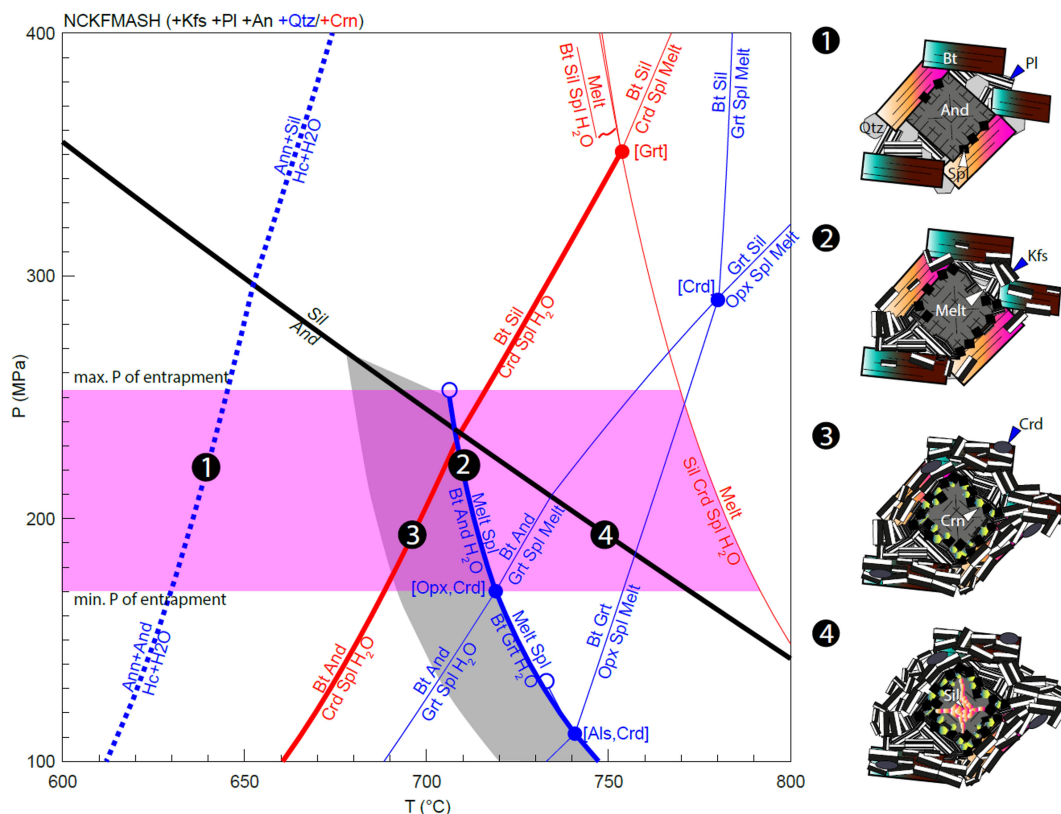
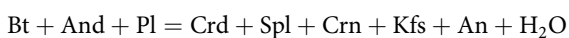


Figure 3. *P*–*T* grid calculated with THERMOCALC (Powell & Holland, 1988), using the ds62 thermodynamic dataset (Holland & Powell, 2011) and activity–composition models for metapelite-forming minerals (White *et al.*, 2014); quartz, anorthite, corundum and H₂O are assumed as pure endmembers. Reactions in blue are calculated for SiO₂-saturated compositions; continuous blue lines are calculated in the NCKFMASH system while broken blue lines are calculated in the NCKFASH system. Reactions in red are calculated for SiO₂-undersaturated compositions. The thick reactions in blue and red (i.e. R1, R2, R3, R4) are those recorded in the andalusite-bearing xenoliths and xenocrysts. The grey area highlights the effect of boron on the wet solidus (modified after Spicer *et al.* 2004). The magenta-filled field highlights the *P* conditions of entrapment and the maximum-*T* conditions reached, limited by the wet solidus in corundum-saturated system. On the right side, frames 1–4 are cartoons representing the evolution of the observed microstructures related to reactions R1–R4. Mineral abbreviations after Kretz (1983).

In this case, as partial melting proceeds, quartz may be consumed, and the system becomes SiO₂-undersaturated. When this happens, melting stops and corundum forms together with K-feldspar, anorthite, spinel and fluid. Consequently, the system becomes corundum-saturated and andalusite is continuously consumed up to reaching reaction R3:



If the position of the wet solidus is poorly affected by boron in the *P*–*T* space and R2 occurs at the highest-*T*, partial melting in the andalusite field will likely take place at higher *T* than R3 (Fig. 3). Once quartz is consumed in R2 and the system becomes SiO₂-undersaturated, biotite and andalusite would be rapidly consumed, since R3 would be largely overstepped. Irrespective of R2 being crossed at lower *T* or at higher *T* than R3, the occurrence of R3 is confirmed by the presence of cordierite together with feldspars around the andalusite xenocryst. A further temperature increase may produce the andalusite to sillimanite transition, R4. The presence of both Al₂SiO₅ phases observed in the xenocryst is evidence of the sluggish reaction kinetics with andalusite surviving in a metastable state in the field of sillimanite (e.g. Droop & Moazzen, 2007).

Considering the *P*–*T* grid (Fig. 3) and the sequence of reactions, the andalusite-bearing xenoliths and xenocrysts were incorporated into the granitic magma at between 170 and 250 MPa, the lowest

pressure defined by where the wet solidus intersects the garnet-forming reactions.

5. Timing of emplacement and exhumation

5.1. U–Pb geochronology

Zircon grains are generally elongated (mean aspect ratio = 3.47). These grains typically have a large homogeneous core and rims/tips with oscillatory zoning (Fig. 4a). We have undertaken forty-seven U–Pb analyses on forty-five different grains. Spot analyses were positioned at the rims with oscillatory zoning and at the cores of some grains. Eleven analyses were discarded as the isotopic signal was severely influenced by apatite inclusions. Except for one grain, which yielded two old dates (early Jurassic and early Cretaceous), all analyses (*n* = 35 from 34 zircon grains) provided ²⁰⁶Pb/²³⁸U ages in the range of 5.0–6.3 Ma (Table 1). The main data population (26 data out of 34) provides a weighted average age of 5.7 ± 0.4 Ma (Fig. 4b). This population corresponds to the central distribution of the data and has been obtained by discarding a few older (four) and younger (four) data interpreted as potential xenocrysts or grains affected by late perturbing events.

5.2. Apatite (U–Th)/He thermochronology

Apatite (U–Th)/He (AHe) analyses were performed on samples from the Giglio granite. Ages, corrected for recoil using Farley

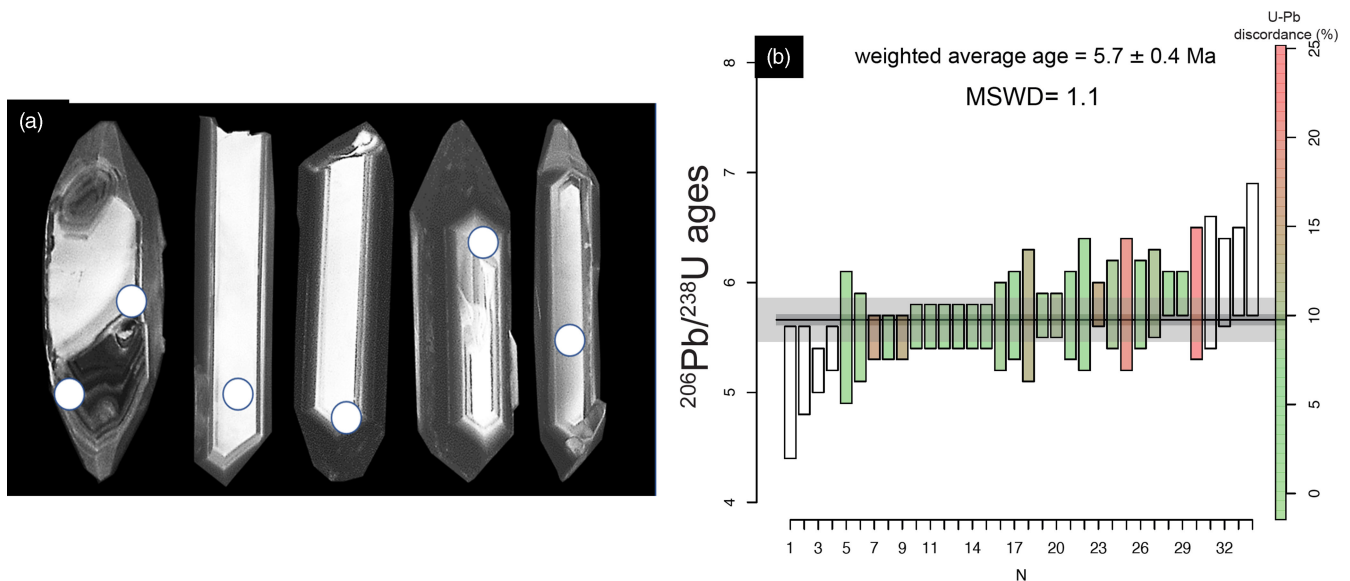


Figure 4. (a) BSE-CL images of zircon grains from granite representative of different CL features. Location of LA-ICP-MS spots is shown and corresponds to 25 μm diameter. (b) $^{206}\text{Pb}/^{238}\text{U}$ zircon data for GIG15 and GIG11 samples. U-Pb data are ordered and shown as vertical bars comprising two sigma errors. The coloured bars were used for calculation of weighted average age (grey horizontal bar). The colour of the bars is related to the percentage of discordance according to right vertical axis scale.

(2002), are reported in Table 2. Two aliquots yielded erroneously old ages, which could have resulted from unrecognized inclusions, ^4He implantation or U-Th zonation (Farley, 2002; Dobson *et al.* 2010). They are not geologically meaningful and were not used in the cooling age calculation. Aliquot AHe ages range from 5.18 to 5.80 Ma. The average age of all aliquots is 5.38 ± 0.2 Ma. This partially overlaps the emplacement age attesting to the rapid exhumation of the pluton.

5.3. Exhumation history

To constrain the exhumation history of the Giglio Island granite, we consider the U-Pb, (U-Th)/He ages and the emplacement depth. Thus, we have two ages in the exhumation history needing to be related to distinct crustal levels. Ideally, the zircon U-Pb age of 5.7 ± 0.4 Ma represents the time when the magma was emplaced at the constrained crustal pressure of 250–170 MPa. On the other hand, the (U-Th)/He age of 5.38 ± 0.2 Ma represents the time of cooling below established closure temperature in response to exhumation (e.g. Spencer *et al.* 2019). To estimate the closure temperature, we followed Reiners (2005). On the basis of the average dimension of apatite crystals (c. 130 μm) and the cooling rate of the granite in approaching the surface (>50 $^{\circ}\text{C}/\text{Myr}$), a closure temperature of c. 80 $^{\circ}\text{C}$ was assumed. To convert this temperature to depth, an understanding of the geothermal gradient at the time is required. Even before the ascent and emplacement of the Giglio granite, the region must have been characterized by a high thermal gradient, precursor of pluton emplacement and result of the lithospheric thinning that affected the northern Tyrrhenian domain. After the emplacement of the granitic magma, this high thermal gradient is further elevated. For example, in the Larderello area, which is underlain by a cooling granitic body, the regional surface heat flow is currently in the order of 200 mW/m^2 (e.g. Batini *et al.* 2003; Bellani *et al.* 2004), in zones mostly affected by conductive heat transport. On this basis, fixing thermal conductivity at 2.5 $\text{W m}^{-1}\text{K}^{-1}$, we obtain a thermal gradient of c. 80 $^{\circ}\text{C}/\text{km}$. Consequently, during the exhumation of the Giglio granite, we speculate that the 80 $^{\circ}\text{C}$ isotherm was located at c. 1 km below the surface. Conservatively, we have fixed the depth of emplacement to

the minimum value of 6.4 km, corresponding to a pressure of 170 MPa. Thus, the minimum amount of exhumation is estimated to be 5.4 km. Considering the exhumation took up to 0.9 Myr (the maximum difference of the zircon U-Pb and apatite (U-Th)/He ages allowed by the uncertainties), the minimum estimate of the average exhumation rate is 6 mm/year up to 1 km below the surface.

6. Discussion

The level of emplacement of the Giglio Island granite as reported in the literature was based on melt composition in the wet granitic system (Westerman *et al.* 1993). In this way, a minimum crystallization pressure of 400 MPa, corresponding to a depth of c. 15 km, was obtained. This is deeper than the estimates of all the other Neogene granites of the TMP, not exceeding 8 km (Acocella & Rossetti, 2002). Nevertheless, the occurrence of miarolitic cavities, which we recognized in the Arenella facies, supports a shallower level of emplacement of the Giglio Island granite (Candela, 1997). This is consistent with the presence of roof pendants and of locally abundant xenoliths derived from the disaggregation of the wall and roof rocks, still indicative of shallow magma intrusion (Clarke, 1992; Philpotts & Ague, 2022). The sequence of reactions we detailed in the present study (Fig. 3), related to the microstructures observed in the xenoliths and xenocrysts (Fig. 2), indicates a pressure range of ~170–250 MPa, corresponding to a depth interval of ~6.4–9.4 km (for average crustal density of 2.7 g/cm^3). Considering that the xenoliths and xenocrysts may be incorporated into the magma even before reaching the final emplacement site, the pluton of the Giglio Island may not be as different as the other granites of the TMP in relation to its original depth of 6.4 km.

The new U-Pb emplacement age of the Giglio Island granite (5.7 ± 0.4 Ma) is significantly older than previous determinations (4.88 ± 0.07 to 5.1 ± 0.15 Ma; Ferrara & Tonarini, 1985; Westerman *et al.* 1993). The emplacement occurred in the late Messinian, not during Pliocene (Cohen *et al.* 2013). This was after the Monte Capanne and Porto Azzurro granites (7.3 ± 0.2 Ma and

Table 2. (U + Th)/He data of apatite from Giglio granite

Sample	Total ⁴ He (cc)	²³⁸ U (ng)	²³² Th (ng)	Th/U	Uncorrected age (Ma)	F _T *	Corrected age
GIG11-2	1.273E-09	0.99	1.88	1.88	7.36	0.89	8.26
GIG11-3	1.174E-09	1.43	2.48	1.72	4.81	0.90	5.32
GIG15-2	5.88E-10	0.97	0.90	0.91	4.10	0.79	5.18
GIG15-3	4.769E-09	7.51	3.74	0.50	4.68	0.89	5.25
GIG15-5	2.571E-09	3.87	1.37	0.35	5.05	0.94	5.40
GIG15-6	7.972E-09	5.91	8.11	1.37	8.39	0.83	5.30
GIG15-7	6.666E-09	6.67	8.62	1.29	6.30	0.83	5.80
GIG15-9	2.037E-09	2.20	1.93	0.87	6.33	0.83	7.60

6.4 ± 0.4 Ma, respectively; Barboni *et al.* 2015, Spiess *et al.* 2021), almost coevally with the Campiglia granite (5.409 ± 0.043 in Di Vincenzo *et al.* 2022) and before the Gavorrano granite (4.9 ± 0.2 Ma; Ferrara & Tonarini, 1985). From the regional perspective, this is in line with the migration of magmatic activity to the E–NE with time (see Fig. 1a). Granite emplacement is believed to be controlled by NE-oriented regional transfer zones, whose activity is coeval with the eastward crustal stretching since Miocene (Dini *et al.* 2008).

The Neogene-Quaternary extensional setting of inner Northern Apennines and Tyrrhenian Sea (e.g. Carmignani *et al.* 1994; Daniel & Jolivet, 1995; Brunet *et al.* 2000; Dini *et al.* 2002; Barchi, 2010; Rossetti *et al.* 2015; Jolivet *et al.* 2021) was challenged by Finetti *et al.* (2001 with references therein) who envisaged a Miocene-Pliocene continuous compressional evolution up to the Pleistocene. Modest differences in the regional stress field through time were introduced by Bonini & Sani (2002) who suggested that the predominant compression was punctuated by short-lived extensional periods in the last 9 Myr. Later, Bonini *et al.* (2014) proposed that, after the Oligocene-early Miocene collisional stage, a significant Miocene extensional phase took place, thinning the crust and lithosphere. However, in the Bonini *et al.*'s hypothesis, shortening was again active between 7.5 and 3.5 Ma, when magmatism took place. In this perspective, the development of thrusts would have caused the emplacement and exhumation of the Neogene granitoids of Tuscany (Musumeci *et al.* 2008; Musumeci & Vaselli, 2012; Musumeci *et al.* 2015; Sani *et al.* 2016; Viola *et al.* 2018; Ryan *et al.* 2021; Papeschi *et al.* 2022). In addition, Sani *et al.* (2016) and Montanari *et al.* (2017) proposed a slightly different scenario where extension, alternated with local compressional events, would have been active during the Pleistocene. Considering the depth of granite emplacement, the compressional deformation would have implied doubling of the crust. However, it is noteworthy that no indication of crustal thickening or high-pressure metamorphic conditions in the granite evolution time range (Messinian-Pliocene) has been recognized, throughout the inner Northern Apennines, from Corsica to Tuscany (Brunet *et al.* 2000; Molli, 2008; Bianco *et al.* 2015; Rossetti *et al.* 2015). More reasons why extensional tectonics better explains the Neogene geological evolution are given in Brogi *et al.* (2005), Brogi (2008), Brogi and Liotta (2008), and Spiess *et al.* (2021).

The new (U-Th)/He age suggests that the exhumation of the Giglio granite was essentially complete before the start of the Pliocene.

The minimum estimate of the average exhumation rate of 6 mm/year is significantly higher than the value (3.4 – 3.9 mm/year) reported by Spiess *et al.* (2021) for the Porto Azzurro granite of eastern Elba. Even higher exhumation rates have been reported

for young granitoids, although in a different geodynamic setting by Spencer *et al.* (2019). Depending on their assumption of geothermal gradient, they estimated exhumation rates spanning from 5 mm to 40 mm/year.

Similar to the setting of the Elba Island, the exhumation of the Giglio Island pluton was favoured by unroofing operated by low-angle extensional detachments (Keller & Pialli, 1990; Smith *et al.* 2011; Spiess *et al.* 2021), related to the development of the Tyrrhenian Basin (Bartole, 1995; Jolivet *et al.* 1998; Rossetti *et al.* 1999). At Elba, Porto Azzurro and Monte Capanne plutons were emplaced along regional transfer zones (Dini *et al.* 2008), up to 6–7 km wide, that separated crustal volumes with different amounts of extension and related vertical movements, coeval with the unroofing low-angle detachments (Smith *et al.* 2011; Liotta *et al.* 2015). A similar scenario has also been documented for the Gavorrano pluton (Brogi *et al.* 2021), inland of southern Tuscany, suggesting that the TMP plutons were subjected to a common mechanism, which controlled the fast uplift of extending crust and the progressive exhumation of the magmatic bodies (Spiess *et al.* 2021, 2022). We can speculate that also the Giglio Island pluton after its emplacement along a transfer zone, with its inland continuation in southern Tuscany (i.e. the Albegna tectonic lineament, Fig. 1a), was rapidly unroofed by low-angle normal faulting (Rossetti *et al.* 1999). This was accompanied by vertical movements favoured by the crustal thermal softening consequent to the upward migration of the regional brittle-ductile transition after magma emplacement, simulated by thermo-rheological modelling for the Elba Island granites (Caggianelli *et al.* 2014; Liotta *et al.* 2015; Spiess *et al.* 2021). A possible scenario for the exhumation of the Giglio granite is illustrated by the schematic diagram of Fig. 5.

Finally, the studies on the sedimentary evolution of the Tyrrhenian Basin indicate syn-rift sedimentation during Miocene-early Pliocene (11–3.6 Ma) and post-rift sedimentation from late Pliocene to present (Bartole, 1995). Early Pliocene deposits filling up the Formiche Basin to the north of Giglio Island (Pascucci *et al.* 1999) onlap the substrate units hosting the granite. This accounts for a limited contribution of erosion to the final stage of exhumation, while the bulk of exhumation occurred earlier, by effects of crustal thermal softening and reduction of the crust thickness by normal fault activity.

7. Concluding remarks

We draw the following conclusions from this work:

- Xenoliths and xenocrysts of the Giglio granite are derived from the disaggregation of wall and roof rocks affected by

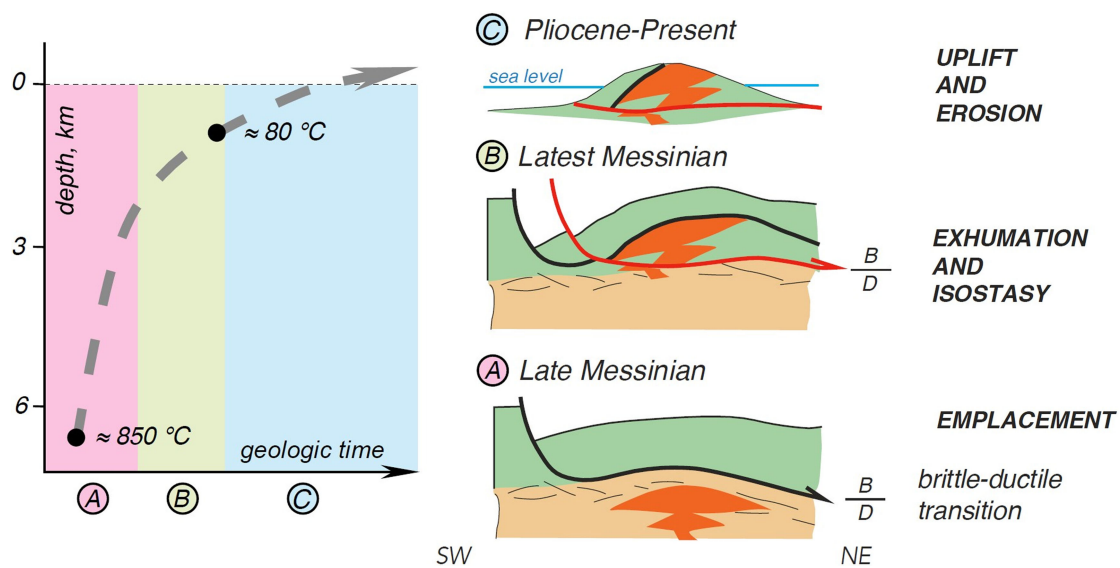


Figure 5. Conceptual sketch of the Giglio Island granite evolution through time. To the left, a possible exhumation path of the granite, according to an exponential law, in line with models set up for the Monte Capanne and Porto Azzurro granites at the Elba Island (Caggianelli *et al.* 2014; Spiess *et al.* 2021). Temperatures of 850 °C and 80 °C are related, respectively, to the emplacement level of the granitic magma and to a depth of c. 1 km, when the closure temperature for AHe is reached. To the right, cartoons illustrating the role of extension and isostasy in determining the exhumation and uplift of the pluton within the transfer zone that favoured magma ascent. The brittle-ductile transition is also qualitatively indicated and is convex upward as an effect of the thermal perturbation produced by the emplacement of the granitic magma (a) in a geodynamic setting affected by crustal stretching since early-middle Miocene. Progressive deformation developed through new normal faults, cross-cutting the previously formed structures and soling out into the brittle-ductile transition, once magma cooling occurred (b). A rapid exhumation resulted in the exposure of the granite during Pliocene (c).

contact metamorphism and characterized by the presence of andalusite ± sillimanite together with biotite, spinel, ilmenite, plagioclase, K-feldspar and cordierite.

- b. The reconstructed reaction sequence that affected the xenoliths and xenocrysts after their incorporation into the magma allowed to constrain pressure in the range of 170 – 250 MPa, corresponding to a minimum emplacement depth of c. 6.4 km for the Giglio Island granite. Thus, in terms of the level of emplacement, it may not be significantly different from the other granites of the TMP.
- c. The new zircon U-Pb age of the Giglio Island granite is 5.7 ± 0.4 Ma, and its emplacement can now be attributed to the latest Messinian.
- d. The AHe cooling age of 5.3 ± 0.2 Ma implies a rapid exhumation with an average rate of 6 mm/year at minimum.
- e. The fast exhumation of the Giglio pluton resulted from the interplay between the exhumation induced by the extending crust, operated by low-angle normal faults and the crustal thermal softening determined by the cooling magma.

Supplementary material. The supplementary material for this article can be found at <https://doi.org/10.1017/S0016756823000420>.

Acknowledgements. This study was conducted in the frame of Chinedu Uduma Ibe's PhD, supported by the University of Bari, Aldo Moro, Italy. We thank Luigia Di Nicola, Stefania Corvo and Matthia Bonazi for providing invaluable assistance in the laboratories. We acknowledge the editorial work of O. Lacombe and the constructive comments we received from an anonymous referee and R. Lanari.

Competing interests. The authors declare no known competing interests.

References

Acocella V and Rossetti F (2002) The role of extensional tectonics at different crustal levels on granite ascent and emplacement: an example from Tuscany (Italy). *Tectonophysics* **354**, 71–83.

Aldighieri B, Gamba A, Groppelli G, Malara F, Pasquare G, Testa B and Wijbrans J (1998) Methodology for the space–time definition of lateral collapse: the evolution model of Capraia Island (Italy). In *Proceedings of International Association for Mathematical Geology* **98**, 79–85.

Barboni M, Annen C and Schoene B (2015) Evaluating the construction and evolution of upper crustal magma reservoirs with coupled U/Pb zircon geochronology and thermal modeling: a case study from the Mt. Capanne pluton (Elba, Italy). *Earth and Planetary Science Letters* **432**, 436–48.

Barchi MR (2010) The Neogene–Quaternary evolution of the Northern Apennines: crustal structure, style of deformation and seismicity. In *Journal of the Virtual Explorer* (eds M Beltrando, A Peccerillo, M Mattei, S Conticelli & D Carlo), vol. **36**. doi: [10.3809/jvirtex.2009.00220paper10](https://doi.org/10.3809/jvirtex.2009.00220paper10).

Barrese E, Della Ventura G, Di Sabatino B, Giampaolo C and Di Lisa A (1987) The thermometamorphic contact aureole around the Isola del Giglio Granodiorite (Tuscany, Italy): petrography and petrogenetical considerations. *Geologica Roma* **26**, 349–57.

Bartole R (1995) The North Tyrrhenian–Northern Apennines post-collisional system: constraints for a geodynamic model. *Terra Nova* **7**, 7–30.

Batini F, Brogi A, Lazzarotto A, Liotta D and Pandeli E (2003) Geological features of Laderello-Travale and Mt Amiata geothermal areas (Southern Tuscany, Italy). *Episodes* **6**, 239–44.

Bellani S, Brogi A, Lazzarotto A, Liotta D and Ranalli G (2004) Heat flow, deep temperatures and extensional structures in the Larderello Geothermal Field (Italy): constraints on geothermal fluid flow. *Journal of Volcanology and Geothermal Research* **132**, 15–29.

Bianco C, Brogi A, Caggianelli A, Giorgetti G, Liotta D and Meccheri M (2015) HP-LT metamorphism in Elba Island: implications for the geodynamic evolution of the inner Northern Apennines (Italy). *Journal of Geodynamics* **91**, 13–25.

Bonini M and Sani F (2002) Extension and compression in the northern Apennines (Italy) hinterland: evidence from the late Miocene–Pliocene Siena-Radicofani Basin and relations with basement structures. *Tectonics* **21**, 1010. doi: [10.1029/2001TC900024](https://doi.org/10.1029/2001TC900024).

Bonini M, Sani F, Stucchi EM, Moratti G, Benvenuti M, Menanno G and Tanini C (2014) Late Miocene shortening of the Northern Apennines back-arc. *Journal of Geodynamics* **74**, 1–31.

- Borsi S, Ferrara G and Tongiorgi E** (1967) Determination with the K/Ar method of the ages of the igneous rocks of Tuscany. *Bulletin of the Geological Society of Italy* **86**, 3–41.
- Boyce JW and Hodges KV** (2005) U and Th zoning in Cerro de Mercado (Durango, Mexico) fluorapatite: insights regarding the impact of recoil redistribution of radiogenic ⁴He on (U–Th)/He thermochronology. *Chemical Geology* **219**, 261–74.
- Boyce JW, Hodges KV, Olszewski WJ, Jercinovic MJ, Carpenter BD, Reiners PW** (2006) Laser microprobe (U–Th)/He geochronology. *Geochimica et Cosmochimica Acta* **70**, 3031–9.
- Brogi A** (2005) Contractual structures as relicts of the Northern Apennines collisional stage recorded in the Tuscan nappe of the Mt. Amiata geothermal area (Italy). *Bulletin of the Italian Geological Society* **4**, 53–64.
- Brogi A** (2008) Kinematics and geometry of Miocene low-angle detachments and exhumation of the metamorphic units in the hinterland of the Northern Apennines (Italy). *Journal of Structural Geology* **30**, 2–20.
- Brogi A, Caggianelli A, Liotta D, Zucchi M, Spina A, Capezzuoli E and Buracchi E** (2021) The Gavorrano Monzogranite (Northern Apennines): an updated review of host rock Protoliths, thermal metamorphism and tectonic setting. *Geosciences* **11**, 124. doi: [10.3390/geosciences11030124](https://doi.org/10.3390/geosciences11030124)
- Brogi A and Liotta D** (2008) Highly extended terrains, lateral segmentation of the substratum, and basin development: the Middle-Late Miocene Radicondoli Basin (inner northern Apennines, Italy). *Tectonics* **27**. doi: [10.1029/2007TC002188](https://doi.org/10.1029/2007TC002188) TC 5002.
- Brunet C, Monié P, Jolivet L and Cadet JP** (2000) Migration of compression and extension in the Tyrrhenian Sea, insights from ⁴⁰Ar/³⁹Ar ages on micas along a transect from Corsica to Tuscany. *Tectonophysics* **321**, 127–55.
- Caggianelli A, Ranalli G, Lavecchia A, Liotta D and Dini A** (2014) Post-emplacement thermo-rheological history of a granite intrusion and surrounding rocks: the Monte Capanne pluton, Elba Island, Italy. In *Deformation Structures and Processes within the Continental Crust* (eds S Llan-Fúnez, A Marcos & F Bastida), vol. **394**, pp. 129–43. London: Geological Society, Special Publication.
- Caggianelli A, Zucchi M, Bianco C, Brogi A and Liotta L** (2018) Estimating P-T metamorphic conditions on the roof of a hidden granitic pluton: an example from the Mt. Calamita promontory (Elba Island, Italy). *Italian Journal of Geosciences* **137**, 238–53.
- Candela PA** (1997) A review of shallow, ore-related granites: textures, volatiles, and ore metals. *Journal of Petrology* **38**, 1619–33.
- Capponi G, Cortesogno L, Gaggero L and Giammarino S** (1997) The Promontorio del Franco (Island of Giglio): a blueschist element in the Tuscan Archipelago (central Italy). *Atti Ticinensi di Scienze della Terra* **39**, 175–92.
- Carmignani L, Decandia FA, Disperati L, Fantozzi PL, Kligfield R, Lazzarotto A, Liotta D and Meccheri M** (2001) Inner northern Apennines. In *Anatomy of an Orogen: the Apennines and Adjacent Mediterranean Basins* (eds GB Vai & IP Martini), pp. 197–213. Dordrecht: Springer. doi: [10.1007/978-94-015-9829-3_14](https://doi.org/10.1007/978-94-015-9829-3_14).
- Carmignani L, Decandia FA, Disperati L, Fantozzi PL, Lazzarotto A, Liotta D and Meccheri M** (1994) Tertiary extensional tectonics in Tuscany (northern Apennines, Italy). *Tectonophysics* **238**, 295–315.
- Carmignani L, Decandia FA, Disperati L, Fantozzi PL, Lazzarotto A, Liotta D and Oggiano G** (1995) Relationships between the Tertiary structural evolution of the Sardinia-Corsica-Provençal domain and the northern Apennines. *Terra Nova* **7**, 128–37.
- Cesare B, Gómez-Pugnaire MT, Sánchez-Navas A and Grobety B** (2002) Andalusite-sillimanite replacement (Mazarrón, SE Spain): a microstructural and TEM study. *American Mineralogist* **87**, 433–44.
- Clarke DB** (1992) *Granitoid Rocks*, Vol. 7. London: Chapman and Hall.
- Clarke DB** (1995) Cordierite in felsic igneous rocks: a synthesis. *Mineralogical Magazine* **59**, 311–25.
- Cohen KM, Finney SC, Gibbard PL and Fan J-X** (2013) The ICS International Chronostratigraphic Chart. *Episodes* **36**, 199–204. URL: <http://www.stratigraphy.org/ICSchart/ChronostratChart2022-10.pdf>
- Dallmeyer RD and Liotta D** (1998) Extension, uplift of rocks cooling ages in thinned continental provinces: the Larderello geothermal area (inner Northern Apennines, Italy). *Geological Magazine* **135**, 193–202.
- Daniel JM and Jolivet L** (1995) Detachment faults and pluton emplacement; Elba Island (Tyrrhenian Sea). *Bulletin de la Société géologique de France* **166**, 341–54.
- Di Stefano R, Bianchi I, Ciaccio MG, Carrara G and Kissling E** (2011) Three-dimensional Moho topography in Italy: new constraints from receiver functions and controlled source seismology. *G-cubed* **12**, 1–15.
- Di Vincenzo G, Vezzoni S, Dini A and Rocchi S** (2022) Timescale of a magmatic-hydrothermal system revealed by ⁴⁰Ar–³⁹Ar geochronology: the Mio-Pliocene Campiglia Marittima system (Tuscany, Italy). *Scientific Reports* **12**, 7128.
- Dini A, Gianelli G, Puxeddu M and Ruggieri G** (2005) Origin and evolution of Pliocene–Pleistocene granites from the Larderello geothermal field (Tuscan magmatic province, Italy). *Lithos* **81**, 1–31. doi: [10.1016/j.lithos.2004.09.002](https://doi.org/10.1016/j.lithos.2004.09.002)
- Dini A, Innocenti F, Rocchi S, Tonarini S and Westerman DS** (2002) The magmatic evolution of the Late Miocene laccolith-pluton-dyke granitic complex of Elba Island Italy. *Geological Magazine* **139**, 257–79.
- Dini A, Westerman DS, Innocenti F and Rocchi S** (2008). Magma emplacement in a transfer zone: the Miocene mafic Orano dyke swarm of Elba Island, Tuscany, Italy. *Geological Society, London, Special Publications* **302**, 131–48.
- Dobson KJ, Stuart FM and Dempster TJ** (2010) Constraining the post-emplacement evolution of the Hebridean Igneous Province (HIP) using low temperature thermochronology: how long has the HIP been cool? *Journal of the Geological Society* **167**, 973–84.
- Droop GT and Moazzen M** (2007) Contact metamorphism and partial melting of Dalradian pelites and semipelites in the southern sector of the Etive aureole. *Scottish Journal of Geology* **43**, 155–79.
- Evans NJ, Byrne JP, Keegan JT and Dotter LE** (2005) Determination of uranium and thorium in zircon, apatite, and fluorite: application to laser (U–Th)/He thermochronology. *Journal of Analytical Chemistry* **60**, 1159–65.
- Farley KA** (2002) (U–Th)/He dating: Techniques, calibrations, and applications. *Reviews in Mineralogy and Geochemistry* **47**, 819–44.
- Ferrara G and Tonarini S** (1985) Radiometric geochronology in Tuscany: results and problems. *Società Italia di Mineralogia e Petrologia* **40**, 111–24.
- Finetti I, Boccaletti M, Bonini M, Del Ben A, Geletti R, Pipan M and Sani F** (2001) Crustal section based on CROP seismic data across the North Tyrrhenian-northern Apennines-Adriatic Sea. *Tectonophysics* **343**, 135–63.
- Foeken JP, Stuart FM, Dobson KJ, Persano C and Vilbert D** (2006) A diode laser system for heating minerals for (U–Th)/He chronometry. *Geochemistry, Geophysics, Geosystems* **7**. doi: [10.1029/2005GC001190](https://doi.org/10.1029/2005GC001190).
- Gardien V, Martelat J-E, Leloup P-H, Mahéo G, Bevilard B, Allemand P, Monié P, Paquette J-L, Grosjean A-S, Faure M, Chelle-Michou C and Fellah C** (2022) Fast exhumation rate during late orogenic extension: the new timing of the Pilat detachment fault (French Massif Central, Variscan belt). *Gondwana Research* **103**, 260–75.
- Gianelli G and Laurenzi MA** (2001) Age and cooling rate of the geothermal system of Larderello. *Transactions Geothermal Resources Council* **25**, 731–5.
- Giuntoli F and Viola G** (2022) A likely geological record of deep tremor and slow slip events from a subducted continental broken formation. *Scientific Reports* **12**, 4506.
- Gola G, Bertini G, Bonini M, Botteghi S, Brogi A, De Franco R and Trumpy E** (2017) Data integration and conceptual modelling of the Larderello geothermal area, Italy. *Energy Procedia* **125**, 300–9.
- Hennig J, Hall R, Forster MA, Kohn BP and Lister GS** (2017) Rapid cooling and exhumation as a consequence of extension and crustal thinning: inferences from the Late Miocene to Pliocene Palu Metamorphic Complex, Sulawesi, Indonesia. *Tectonophysics*, **712**, 600–22.
- Holland TJB and Powell R** (2011) An improved and extended internally consistent thermodynamic dataset for phases of petrological interest, involving a new equation of state for solids. *Journal of Metamorphic Geology* **29**, 333–83.
- Horstwood MS, Foster GL, Parrish RR, Noble SR and Nowell GM** (2003) Common- Pb corrected in situ U–Pb accessory mineral geochronology by LA-MC-ICP-MS. *Journal of Analytical Atomic Spectrometry* **18**, 837–46. doi: [10.1039/B304365G](https://doi.org/10.1039/B304365G).
- Innocenti F, Serri G, Ferrara G, Manetti P and Tonarini S** (1992) Genesis and classification of the rocks of the Tuscan magmatic province: thirty years after Marinelli's model. *Acta Vulcanologica* **2**, 247–65.

- Innocenti F, Agostini S, Di Vincenzo G, Doglioni C, Manetti P, Savain MY and Tonarini S (2005) Neogene and Quaternary volcanism in Western Anatolia: magma sources and geodynamic evolution. *Marine Geology* **221**, 397–421.
- Ito H, Yamada R, Tamura A, Arai S, Horie K and Hokada T (2013) Earth's youngest exposed granite and its tectonic implications: the 10–0.8 ma Kurobegawa granite. *Scientific Reports* **3**. doi: [10.1038/srep01306](https://doi.org/10.1038/srep01306)
- Jackson SE, Pearson NJ, Griffin WL and Belousova EA (2004) The application of laser ablation-inductively coupled plasma-mass spectrometry to in situ U–Pb zircon geochronology. *Chemical Geology* **211**, 47–69. doi: [10.1016/j.chemgeo.2004.06.017](https://doi.org/10.1016/j.chemgeo.2004.06.017).
- Jiao R, Herman F and Seward D (2017) Late Cenozoic exhumation model of New Zealand: impacts from tectonics and climate. *Earth-Science Reviews* **166**, 286–98.
- Johnson JB, Aster RC and Kyle PR (2004) Volcanic eruptions observed with infrasound. *Geophysical Research Letters* **31**, 1123.
- Jolivet L, Arbaret L, Le Pourthiet L, Cheval-Garabedian F, Roche V, Rabillard A and Labrousse L (2021) Interactions of plutons and detachments comparison between Aegean and Tyrrhenian granitoids. *Solid Earth* **12**, 1357–88. doi: [10.5194/se-12-1357-2021](https://doi.org/10.5194/se-12-1357-2021).
- Jolivet L, Faccenna C, Goffé B, Mattei M, Rossetti F, Brunet C and Parra T (1998) Mid-crustal shear zones in postorogenic extension: example from the northern Tyrrhenian Sea. *Journal of Geophysical Research: Solid Earth* **103**, 12123–60.
- Jolivet L, Sautter V, Moretti I, Vettor T, Papadopoulou Z, Augier R, Denèle Y and Arbaret L (2021) Anatomy and evolution of a migmatite-cored extensional metamorphic dome and interaction with syn-kinematic intrusions, the Mykonos-Delos-Rheneia MCC. *Journal of Geodynamics* **144**, 101824.
- Keller JVA and Piali G (1990) Tectonics of the Island of Elba: a reappraisal. *Bollettino della Società Geologica Italiana* **109**, 413–25.
- Kretz R (1983) Symbols for rock-forming minerals. *American Mineralogist* **68**, 277–9.
- Lanari R, Boutoux A, Faccenna C, Herman F, Willett SD and Ballato P (2023) Cenozoic exhumation in the Mediterranean and the Middle East. *Earth-Science Reviews* **237**, 104328.
- Lazarotto A, Mazzanti R and Mazzoncini F (1964) Geologia del promontorio Argentario (Grosseto) e del promontorio del Franco (Isola del Giglio-Grosseto). *Bollettino della Società Geologica Italiana* **83**, 1–124.
- Liotta D, Brogi A, Meccheri M, Dini A, Bianco C and Ruggieri G (2015) Coexistence of low-angle normal and high-angle strike-to oblique-slip faults during Late Miocene mineralization in eastern Elba Island (Italy). *Tectonophysics* **660**, 17–34.
- Ludwig KR (2003) *User's Manual for Isoplot 3.00: A Geochronological Toolkit for Microsoft Excel*. Kenneth R. Ludwig, Berkeley Geochronology Centre, Special publication, **4**, 74.
- McDowell FW, McIntosh WC and Farley KA (2005) A precise 40Ar–39Ar reference age for the Durango apatite (U–Th)/He and fission-track dating standard. *Chemical Geology* **214**, 249–63.
- Meesters AGCA and Dunai TJ (2005) A noniterative solution of the (U–Th)/He age equation. *Geochemistry, Geophysics, Geosystems* **6**, Q04002.
- Moeller S, Grevemeyer I, Ranero CR, Berndt C, Klaeschen D, Sallarès V and de Franco R (2013) Early-stage rifting of the northern Tyrrhenian Sea Basin: results from a combined wide-angle and multichannel seismic study. *Geochemistry, Geophysics, Geosystems* **14**, 3032–52.
- Molli G (2008) Northern Apennines Corsica orogenic system: an updated overview. *Journal of the Geological Society Special Publication* **298**, 413–42. doi: [10.1144/SP298.19](https://doi.org/10.1144/SP298.19).
- Montanari D, Minissale A, Doveri M, Gola G, Trumpy E, Santilano A and Manzella A (2017) Geothermal resources within carbonate reservoirs in western Sicily (Italy): a review. *Earth-Science Reviews* **169**, 180–201.
- Montanari D, Ruggieri G, Bonini M and Balestrieri ML (2023) First application of low temperature thermochronology as a tool for geothermal exploration: a promising, preliminary test from the Larderello-Travale geothermal field (Italy). *Geothermics* **107**, 102603.
- Musumeci G, Mazzarini F and Barsella M (2008) Pliocene crustal shortening on the Tyrrhenian side of the northern Apennines: evidence from the Gavorrano antiform (southern Tuscany, Italy). *Journal of the Geological Society* **165**, 105–14.
- Musumeci G, Mazzarini F and Cruden AR (2015) The Zuccale Fault, Elba Island, Italy: a new perspective from fault architecture. *Tectonics* **34**, 1195–218. doi: [10.1002/2014TC003809](https://doi.org/10.1002/2014TC003809).
- Musumeci G and Vaselli L (2012) Neogene deformation and granite emplacement in the metamorphic units of northern Apennines (Italy): insights from mylonitic marbles in the porto Azzurro pluton contact aureole (Elba island). *Geosphere* **8**, 470–90. doi: [10.1130/ges00665.1](https://doi.org/10.1130/ges00665.1)
- Papeschi S, Vannucchi P, Hirose T and Okazaki K (2022) Deformation and material transfer in a fossil subduction channel: evidence from the Island of Elba (Italy). *Tectonics* **41**. doi: [10.1029/2021TC007164e2021TC007164](https://doi.org/10.1029/2021TC007164e2021TC007164).
- Pascucci V, Merlini S and Martini IP (1999) Seismic stratigraphy of the Miocene-Pleistocene sedimentary basins of the Northern Tyrrhenian Sea and western Tuscany (Italy). *Basin Research* **11**, 337–56.
- Pattison DRM and Harte B (1988) Evolution of structurally contrasting anatectic migmatites in the 3-kbar Ballachulish aureole, Scotland. *Journal of Metamorphic Geology* **6**, 475–94.
- Philpotts AR and Ague JJ (2022) *Principles of Igneous and Metamorphic Petrology*. Shaftesbury road, United Kingdom: Cambridge University Press.
- Pichavant M (1981) An experimental study of the effect of boron on a water saturated haplogranite at 1 Kbar vapour pressure: Geological applications. *Contributions to Mineralogy and Petrology* **76**, 430–9.
- Poli ME, Peruzza L, Rebez A, Renner G, Slejko D and Zanferrari A (2002) New seismotectonic evidence from the analysis of the 1976–1977 and 1977–1999 seismicity in Friuli (NE Italy). *Bollettino di Geofisica Teorica ed Applicata* **43**, 53–78.
- Powell R and Holland TJB (1988) An internally consistent dataset with uncertainties and correlations: 3. Applications to geobarometry, worked examples and a computer program. *Journal of Metamorphic Geology* **6**, 173–204.
- Reiners PW (2005) Zircon (U–Th)/He thermochronometry. *Reviews in Mineralogy and Geochemistry* **58**, 151–79.
- Ricceri F and Stea B (1992) Geophysical presence of a deep-seated «granitic stock» in the Massa Marittima mining district (Grosseto, southern Tuscany): metallogenic implications. *Newsletter* **5**, 391–400.
- Rochira F, Caggianelli A and de Lorenzo S (2018) Regional thermo-rheological field related to granite emplacement in the upper crust: implications for the Larderello area (Tuscany, Italy). *Geodinamica Acta* **30**, 225–40.
- Romagnoli P, Arias A, Barelli A, Cei M and Casini M (2010) An updated numerical model of the Larderello–Travale geothermal system. Italy. *Geothermics* **39**, 292–313.
- Rossetti F, Faccenna C, Jolivet L, Funicello R, Tecce F and Brunet C (1999) Syn- versus post orogenic extension: the case study of Giglio Island (Northern Tyrrhenian Sea, Italy). *Tectonophysics* **304**, 71–93.
- Rossetti F, Glodny J, Theye T and Maggi M (2015) Pressure–temperature–deformation–time of the ductile Alpine shearing in Corsica: from orogenic construction to collapse. *Lithos* **218–219**, 99–116.
- Ryan E, Papeschi S, Viola G, Musumeci G, Mazzarini F, Torgersen E, Sørensen BE and Ganerød M (2021) Syn-Orogenic exhumation of high-P units by upward extrusion in an Accretionary wedge: insights from the eastern Elba Nappe Stack (Northern Apennines, Italy). *Tectonics* **40**. doi: [10.1029/2020tc006348](https://doi.org/10.1029/2020tc006348).
- Saki A (2010) Mineralogy, geochemistry and geodynamic setting of the granitoids from NW Iran. *Geological Journal* **45**, 451–66.
- Sani F, Bonini M, Montanari D, Moratti G, Corti G and Ventisette CD (2016) The structural evolution of the Radicondoli–Volterra Basin (southern Tuscany, Italy): relationships with magmatism and geothermal implications. *Geothermics* **59**, 38–55.
- Serri G, Innocenti F and Manetti P (1993) Geochemical and petrological evidence of the subduction of delaminated Adriatic continental lithosphere in the genesis of the Neogene-Quaternary magmatism of central Italy. *Tectonophysics* **223**, 117–214.
- Sláma J, Košler J, Condon DJ, Crowley JL, Gerdes A, Hanchar JM, Horstwood MSA, Morris GA, Nasdala L, Norberg N, Schaltegger U, Schoene B, Tubrett MN and Whitehouse MJ (2008) Plešovice zircon — a new natural reference material for U–Pb and Hf isotopic microanalysis. *Chemical Geology* **249**, 1–35.

- Smith SAF, Holdsworth RE and Collettini C (2011) Interactions between low-angle normal faults and plutonism in the upper crust: insights from the Island of Elba, Italy. *Bulletin* **123**, 329–46.
- Spencer CJ, Danišik M, Ito H, Hoiland C, Tapster S, Jeon H and Evans NJ (2019) Rapid exhumation of earth's youngest exposed granites driven by subduction of an oceanic arc. *Geophysical Research Letters* **46**, 1259–67. doi: [10.1029/2018gl080579](https://doi.org/10.1029/2018gl080579)
- Spicer EM, Stevens G and Buick IS (2004) The low-pressure partial-melting behaviour of natural boron-bearing metapelites from the Mt. Stafford area, central Australia. *Contributions to Mineralogy and Petrology* **148**, 160–79.
- Spies R, Langone A, Caggianelli A, Stuart FM, Zucchi M, Bianco C and Liotta D (2021) Unveiling ductile deformation during fast exhumation of a granitic pluton in a transfer zone. *Journal of Structural Geology* **147**, 104326. doi: [10.1016/j.jsg.2021.104326](https://doi.org/10.1016/j.jsg.2021.104326).
- Spies R, Langone A, Caggianelli A, Stuart FM, Zucchi M, Bianco C, . . . Liotta D (2022) Reply to Mazzarini et al. comment on 'Unveiling ductile deformation during fast exhumation of a granitic pluton in a transfer zone'. *Journal of Structural Geology* **155**, 104498.
- Van Achterbergh E, Ryan CG, Jackson SE and Griffin WL (2001) Laser-Ablation-ICPMS in the earth sciences: principles and applications. *Data reduction software for LA-ICP-MS* **29**, 239–43.
- Vermeech P (2018) IsoplotR: a free and open toolbox for geochronology. *Geoscience Frontiers* **9**, 1479–93. doi: [10.1016/j.gsf.2018.04.001](https://doi.org/10.1016/j.gsf.2018.04.001).
- Viola G, Torgersen E, Mazzarini F, Musumeci G, van der Lelij R, Schönenberger J and Garofalo PS (2018) New constraints on the evolution of the inner Northern Apennines by K-Ar dating of Late Miocene-Early Pliocene compression on the Island of Elba, Italy. *Tectonics* **37**, 3229–43.
- Westerman D, Innocenti F, Tonarini S and Ferrara G (1993) The Pliocene intrusion of island of Giglio. *Memorie della Società Geologica Italiana* **49**, 345–63.
- White RW, Powell R and Johnson TE (2014) The effect of Mn on mineral stability in metapelites revisited: new a-x relations for manganese-bearing minerals. *Journal of Metamorphic Geology* **32**, 809–28.
- Žák J, Verner K, Finger F, Faryad SW, Chlupáčová M and Veselovský F (2011) The generation of voluminous S-type granites in the Moldanubian unit, Bohemian Massif, by rapid isothermal exhumation of the metapelitic middle crust. *Lithos* **121**, 25–40.